Journal of Luminescence 217 (2020) 116774

Contents lists available at ScienceDirect

Journal of Luminescence

journal homepage: http://www.elsevier.com/locate/jlumin

Fluorescence of functionalized graphene quantum dots prepared from infrared-assisted pyrolysis of citric acid and urea

Siyong Gu [a], Chien-Te Hsieh [b,c,*], Chun-Yao Yuan [b], Yasser Ashraf Gandomi [d], Jeng-Kuei Chang [e,**], Chun-Chieh Fu [f], Jou-Wen Yang [f], Ruey-Shin Juang [f,g,***]

[a] Fujian Provincial Key Laboratory of Functional Materials and Applications, School of Materials Science and Engineering, Xiamen University of Technology, Xiamen 361024, China
[b] Department of Chemical Engineering and Materials Science, Yuan Ze University, Taoyuan 32003, Taiwan
[c] Department of Mechanical, Aerospace, and Biomedical Engineering, University of Tennessee, Knoxville, TN 37996, United States
[d] Department of Chemical Engineering, Massachusetts Institute of Technology, Cambridge, MA 02142, United States
[e] Department of Materials Science and Engineering, National Chiao Tung University, Hsinchu 30010, Taiwan
[f] Department of Chemical and Materials Engineering, Chang Gung University, Guishan, Taoyuan 33302, Taiwan
[g] Division of Nephrology, Department of Internal Medicine, Chang Gung Memorial Hospital, Linkou, Taiwan

ARTICLE INFO

Keywords:
Infrared carbonization
Graphene quantum dots
Fluorescence emission
Thermal pyrolysis
Nitrogen doping

ABSTRACT

This paper reports an efficient fabrication of N-doped graphene quantum dots (GQDs) showing controllable chemical and fluorescence (FL) properties through infrared carbonization (IRC) of citric acid and urea. The GQDs prefer to form an equilibrium shapes of circle with an average particle size ranged from 5 to 10 nm. The N/C atomic ratio in GQDs can be precisely tailored in a range from 21.6 to 49.6 at.% by simply controlling the weight ratio of citric acid to urea. With increasing the urea content, the GQDs not only contain N-doped graphene but also incorporate with crystalline cyanuric acid, forming a binary crystallinity. The quantum yield of 22.2% is achieved by N-doped GQDs, prepared from the IRC synthesis of chemical precursor at the citric acid/urea at 3:1. Excessive N and cyanuric acid can lead to FL quenching, red shift and wide spectral distribution. The design of GQDs possesses a multiple chromophoric band-gap structure, originated from the presence of cyanuric acid, defect-related emissive traps, and functional group distributions. This work offers an effective and inspiring approach to engineering both chemical compositions and unique crystalline structures of GQDs, and will therefore facilitate their fundamental research and applications to optical, sensing, energy and biological fields.

1. Introduction

Graphene, as the two-dimensional (2D) monolayer form of sp [2]-hybridized carbon, has attracted wide-ranging interest due to its feasible applications in electronic devices [1], composite materials [2], and semiconductors [3]. By converting 2D graphene sheets into zero-dimensional (0D) graphene quantum dots (GQDs), GQDs serve as one type of 0D nanomaterials with characteristics derived from both graphene and carbon nanodots, regarded as small pieces of graphene [4–6]. Usually, GQDs, like small graphene flakes smaller than 100 nm in size and less than 10 layers in thickness, have interesting optical properties due to quantum confinement and edge effects [6] and tunable surface chemistry [7]. As an emerging attractive carbon material, GQDs have shown their value-added function in electrochemical capacitors [4,8], solar cells [9,10], Li-ion batteries [11,12], photocatalysts [13,14], optical detection probes [15], and bio-imaging probes [16].

In the pioneer research on GQDs, tremendous efforts have been made to develop methods for the preparation of GQDs with controllable particle size, high production yield, low cost, and adjustable surface functionalization [17–23]. Basically, the preparation methods of GQDs can be divided into two categories: top-down and bottom-up methods [5]. The strategy of top-down methods is to convert graphene sheets, carbon nanotubes, carbon fibers or graphite into small pieces of graphene sheet, whereas small molecules are employed as vapor-phase precursor to

* Corresponding author. Department of Chemical Engineering and Materials Science, Yuan Ze University, Taoyuan 32003, Taiwan.
** Corresponding author. Department of Materials Science and Engineering, National Chiao Tung University, Hsinchu 30010, Taiwan.
*** Corresponding author. Department of Chemical and Materials Engineering, Chang Gung University, Guishan, Taoyuan 33302, Taiwan.
E-mail addresses: cthsieh@saturn.yzu.edu.tw (C.-T. Hsieh), jkchang@nctu.edu.tw (J.-K. Chang), rsjuang@mail.cgu.edu.tw (R.-S. Juang).

https://doi.org/10.1016/j.jlumin.2019.116774
Received 6 June 2019; Received in revised form 25 August 2019; Accepted 23 September 2019
Available online 24 September 2019

construct GQDs in bottom-up methods. Recently, thermal pyrolysis of carbon precursors delivers a straightforward pathway to synthesize high-quality GQDs [24,25]. The thermal pyrolysis method takes advantages of its low cost, time saving, and high yield, facilitating large-quantity production of GQDs [26]. To the best of our knowledge, there are few studies reporting as-prepared GQDs with a spherical form via thermal pyrolysis of carbon precursors under IR irradiation and exploring their properties.

Herein this work proposes an efficient pyrolysis method to carbonize low-cost citric acid + urea solid mixture under infrared (IR) irradiation. The IR-assisted carbonization (IRC) method is capable of synthesizing GQDs from solid precursors at low temperatures (i.e., 200 °C) within a short period (20 min). Interestingly, as-prepared GQDs not only behave O- and N-functionalization at edge, on basal plane or into C═C sp [2]-network but also associated with crystalline cyanuric acid. Accordingly, this work aims at exploring the influence of precursor recipe on both surface amidation/oxidation level and tunable fluorescence (FL) emission of GQDs at the first time. To describe the tunable FL, we speculate on key issues and multiple band-gap structure for tailoring FL emissions and quantum yields from functionalized GQD suspension.

2. Experimental section

2.1. IRC synthesis of N-doped GQDs

The growth procedure of GQDs using the IRC method could be briefly described as follows. First, two kinds of precursors, citric acid ($C_6H_8O_7$, molecular weight: 180, purity: 99%) and urea (CON_2H_4, molecular weight: 60, purity: 99%) were uniformly mixed in a 2D mixer at 500 rpm using Zr balls for 30 min. Five solid mixtures contained the weight ratios of citric acid to urea at 3:1, 2:1, 1:1, 1:2, and 1:3, which were designed to sample A, B, C, D, and E, respectively. Each sample (5 g) was carefully placed in thermally resistive glass pan (Pyrix glass) and then put it in a home-made IR furnace. The IR furnace was equipped with six medium-wave IR heater with near-IR wavelength region of 1.4–3.2 μm. Each IR filament was able to exhibit a maximum power density of 80 kW/m^2. The heaters were composed of metallic wire as filament and quartz tube as cover. The near-IR heaters were capable of transferring energy to a body through electromagnetic radiation, i.e., no contact or medium between the two bodies for the energy transfer [27]. The IRC process was composed of three steps: (i) ramping from ambient temperature to 200 °C at 6 °C/min, (ii) isothermal at 200 °C for 20 min, and (iii) natural cooling from 200 °C to ambient temperature. All steps mentioned above were carried out in air without introducing any gas flow.

One thermal treatment in H_2-containing atmosphere was adopted to purify all samples. All samples were placed in the IR furnace again and the thermal purification process was performed in vol.% H_2 + 95 vol.% Ar mixture gas. The thermal process consisted of three steps: (i) ramping from ambient temperature to 200 °C at 3 °C/min, (ii) isothermal at 200 °C for 40 min, and (iii) natural cooling from 200 °C to ambient temperature. The thermally-treated samples were designated to sample F, G, H, I and J, originated from sample A, B, C, D and E, respectively. Prior to any test, all samples were slightly ball-milled and sieved through a stainless foil mesh (Type: 200 mesh). After that, all samples were individually dispersed and washed in distilled water. The samples were finally centrifuged and collected at 15,000 rpm for 10 min.

2.2. Materials characterization of functionalized GQDs

High-resolution transmission electron microscopy (HR-TEM) micrographs were taken using a FEI Talos F200s electron microscope at an accelerating voltage of 200 kV. Ultraviolet–visible absorption spectra were obtained using an Agilent Cary 60 spectrometer, in which the wavelength scan rate was set at 60 nm/min. Each GQD suspension was prepared by dispersing a solid (100 mg) into 1000 mL solvent. Fourier-transform IR (FT-IR) spectra were acquired on Nicolet 380 spectrometer. X-ray diffraction (XRD) measurements were performed by an automated X-ray diffractometer (Rigaku, D/MAX 2500) with Cu-Kα radiation. The graphitization degree of GQD samples was analyzed using Raman spectroscopy (Renishaw Micro-Raman spectrometer). X-ray photoelectron spectroscopy (XPS, Fison VG ESCA210) equipped with Mg-Kα radiation emitter, was used to characterize chemical composition of the samples. The C 1s, N 1s and O 1s spectra were deconvoluted by using a non-linear least squares fitting program with a symmetric Gaussian function.

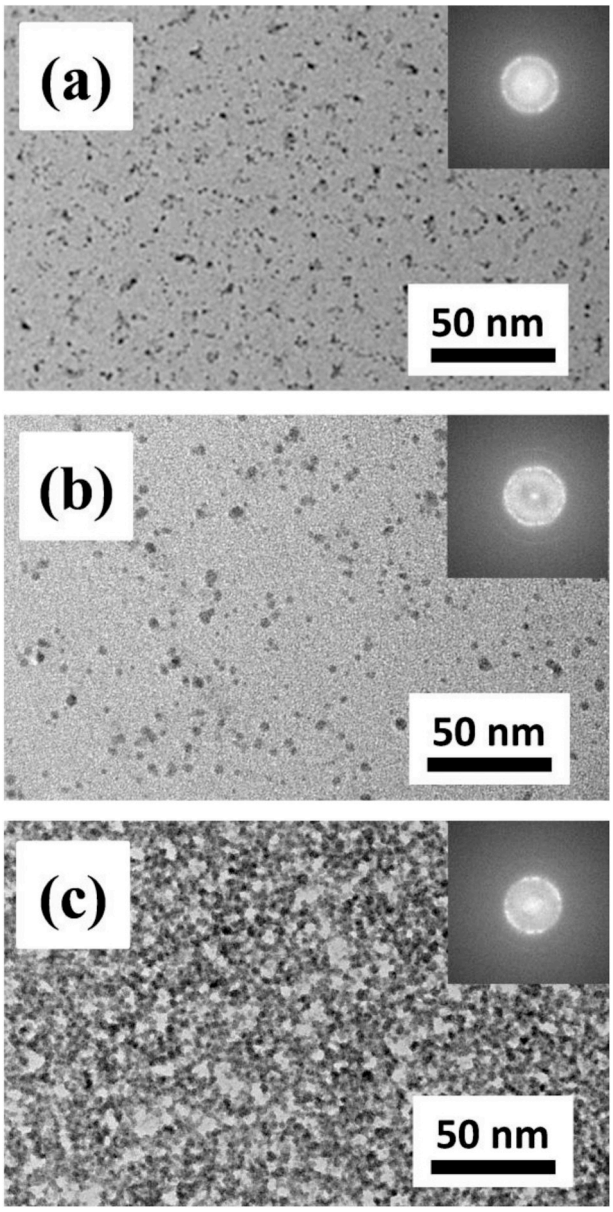

Fig. 1. FE-SEM images and HR-TEM micrographs of N-doped GQDs prepared by the IRC method using different precursors with the weight ratio of citric acid to urea: (a) 2:1, (b) 1:1, and (c) 1:2. The insets of Fig. 1(a), (b), and 1(c) show selected area diffraction patterns, focusing on their GQD samples.

As to FL behavior, all GQD suspensions were ultrasonically vibrated in distilled water bath at ambient temperature for 10 min to ensure homogeneous dispersion. The GQD were super hydrophilic and all suspensions formed were very stable. The FL emission spectra of each suspension were acquired using a fluorescence spectrometer (Hitachi F-7000 FLS920P) at 360 nm. The quantum yield (η) of the sample was measured, referred to Coumarin ($C_9H_6O_2$, molecular weight: 146) reference (η: 73% at 373 nm excitation). The η value of each GQD sample

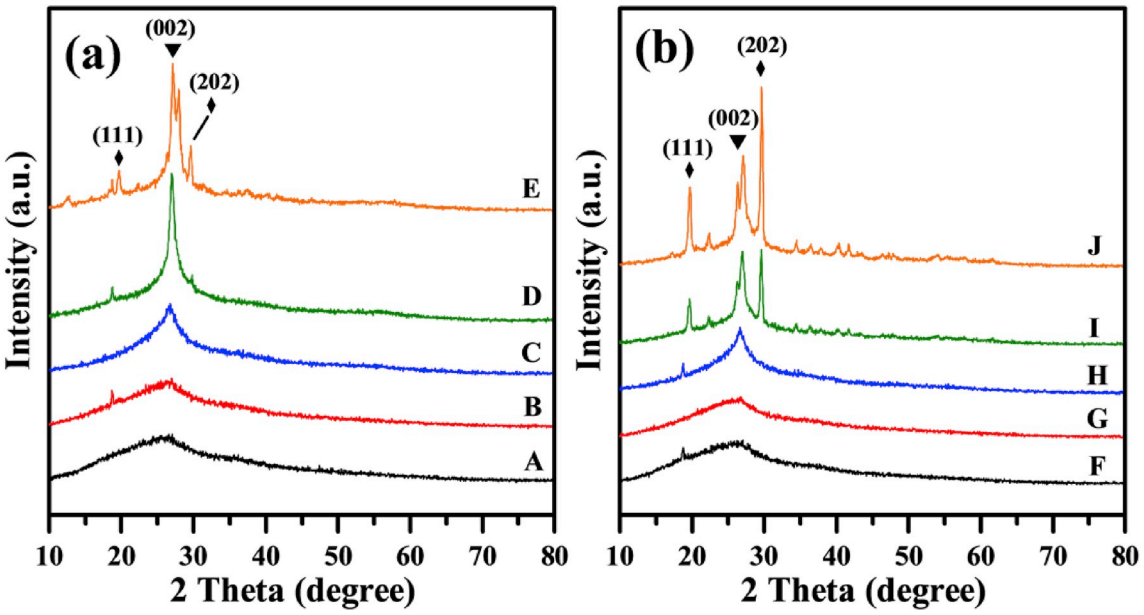

Fig. 2. Typical XRD patterns of (a) A–E (with IRC synthesis) and (b) F–J sample (with IRC synthesis followed by thermal treatment in hydrogen).

was determined by the equation:

$$\eta = \eta_r \times \left[(\text{FL area}/\text{OD})_s/(\text{FL area}/\text{OD})_r\right] \times \Phi_\sigma^2/\Phi_r^2 \quad (1)$$

where the s and r subscripts represent the GQD sample and the reference (i.e., Coumarin), respectively. Herein Φ represents the reflective index of solvent, and FL area and OD are the FL spectral area and absorbance value, respectively.

3. Results and discussion

To determine the possibility of mass production of functionalized GQDs, the production yield was evaluated by the weight ratio of as-prepared GQDs to chemical precursors. The production yield displays an increasing function of citric acid content in the precursor, i.e., sample A (43.2 wt%) > B (42.1 wt%) > C (40.7 wt%) > D (38.2 wt%) > E (35.7 wt%). Since the unit prices of both chemical precursors are low, this result demonstrates that the IRC method exhibits a commercial feasibility in producing highly added-valued GQDs in large scale. HR-TEM studies were carried out on the observation of spherical GQDs (i.e., sample B, C, and D), as shown in Fig. 1(a)–1(c). The images reveal that a large number of GQDs tends to get good uniformity, in which each particle possesses a quasi-spherical shape with a diameter ranging from 5 to 10 nm. Since all samples are found to have identical particle size, the influence of precursor recipe (i.e., the weight ratio of citric acid to urea) on the morphology of as-prepared GQDs seems to be insignificant. An average particle size of graphene-like shape is approximately 5–10 nm for all GQDs, indicating the carbon walls possibly consist of >20 graphene layers. HR-TEM micrographs of B, C, and D samples are also shown in the Electronic Supporting Information (see Fig. S1(a)–S1(c)). The GQD particles display good crystallinity with a lattice distance of *ca.* 0.22 nm, corresponding to the (1120) lattice fringes of graphene sheets [28]. The crystallinity of GQDs was characterized by selected area diffraction (SAD), as shown in inset of Fig. 1(a)–1(c). The SAD patterns

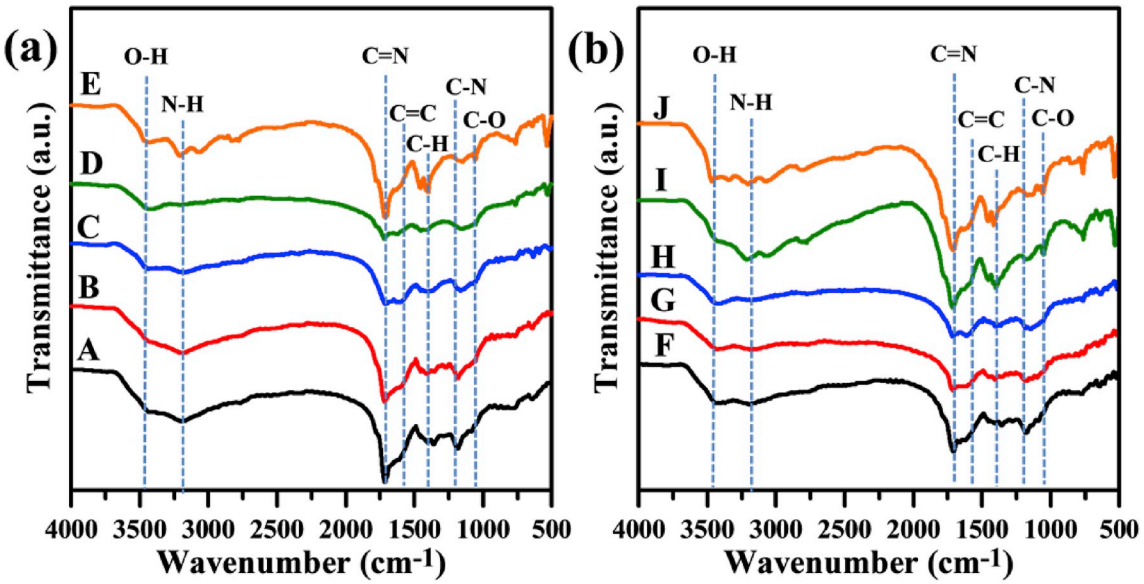

Fig. 3. FT-IR spectra of (a) A–E (with IRC synthesis) and (b) F–J sample (with IRC synthesis followed by thermal treatment in hydrogen).

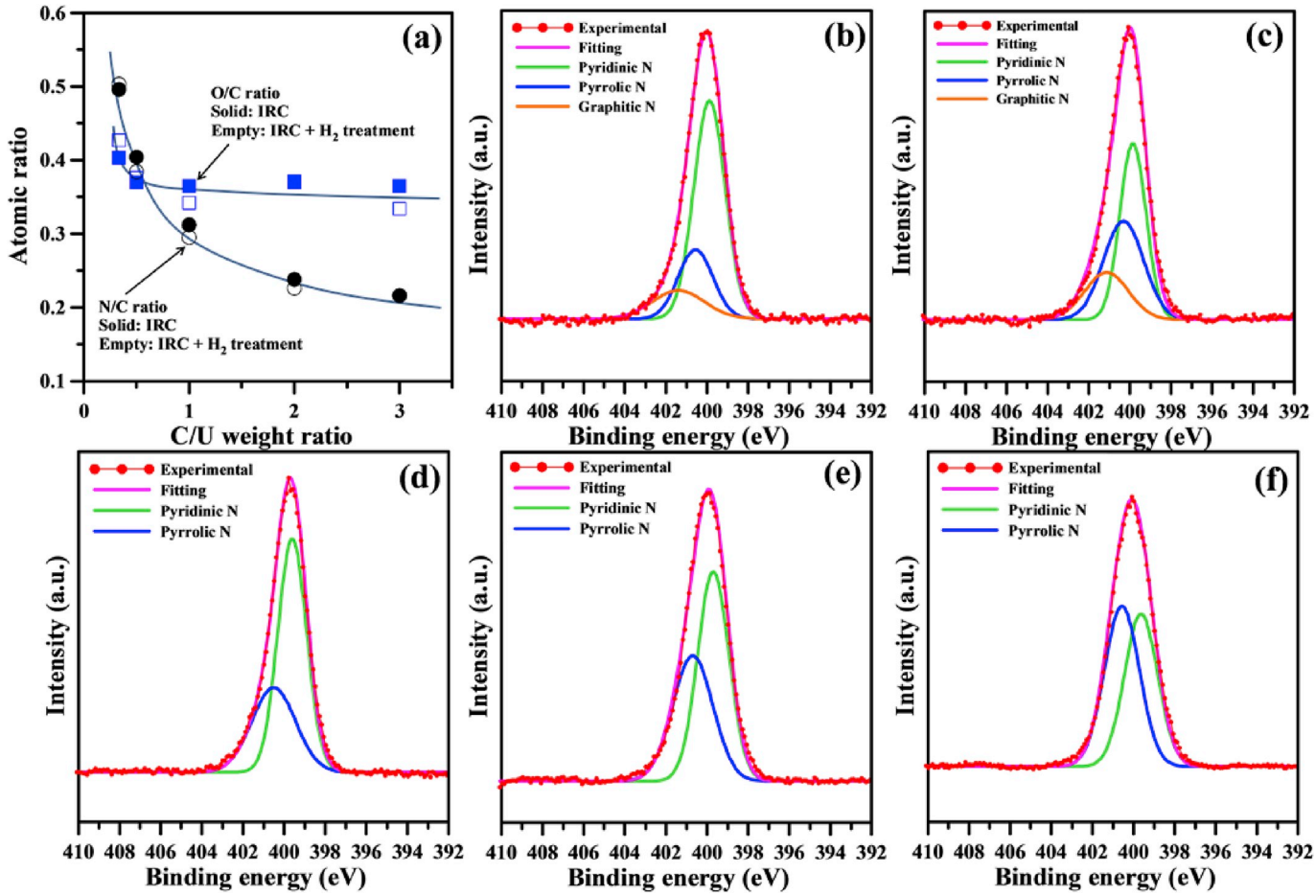

Fig. 4. (a) Variation of atomic ratio with the weight ratio of citric acid to urea (C/U weight ratio). The N 1s spectra of (b) A, (c) B, (d) C, (e) D, and (f) E sample, deconvoluted by a multiple Gaussian function.

where only several circular rings are detected, indicates that all GQDs are of polycrystalline domain within the selected area.

Typical XRD was employed to analyze the crystalline structure of GQD samples, as illustrated in Fig. 2(a) and (b). We observe that 1 $d_{(002)}$ main peak takes place at 26.6–27.1° (JCPDS Card No.: 41–1487) for all samples, confirming the presence of crystalline graphite-like structure. The peak intensity notably increases with decreasing the weight ratio of citric acid in precursor, implying an enhanced crystallinity with aid of urea during the IRC process. According to the calculation of Bragg's Law, the interlayer spacing distances of as-prepared GQDs fall into the range between 0.328 and 0.334 nm, which are very close to that of perfect graphite: 0.335–0.340 nm [29]. It is worth noting that the crystallinity of A–E samples shows a little influence as compared to that of F–J ones, indicating that the thermal reduction in H_2-containing atmosphere is independent to the crystallinity and morphology of GQDs. Interestingly, two reflection bands appear at 19.6 and 29.5° for sample D, E, I and J, mainly originated from the (111) and (202) crystalline planes of cyanuric acid (JCPDS Card No.: 23–1637), respectively. This finding reveals that the $(CNOH)_3$ crystals are prone to be grown at high urea content (i.e., weight ratio of citric acid/urea: 1:2 and 1:3) under IR irradiation. Accordingly, D, E, I and J samples not only contain functionalized GQDs but also incorporated with crystalline $(CNOH)_3$, forming a binary crystalline composite of graphene dot and cyanuric acid.

To further evaluate the crystalline structure, typical Raman spectra of the GQD samples are given in Fig. S2. Two main peaks are identified in the Raman spectra: the *D* band (1350 cm^{-1}) and the *G* band (1580 cm^{-1}). The Raman band observed at 1580 cm^{-1} is ascribed to a single crystallite of graphite (*G* band), whereas the *D* band at 1350 cm^{-1} is commonly attributed to amorphous carbon or deformation vibrations of a hexagonal ring [30–32]. The intensity ratio of *D* to *G* bands can be considered as an indicator of the graphitic degree of carbon-based materials. As shown, the *D/G* ratios of the GQD samples range from 0.99 to 1.02. This result reveals that all the samples synthesized via the IRC method possess a similar crystalline microstructure, confirming a non-detrimental influence of the precursor configuration (i.e., the weight ratio of citric acid to urea) on the crystallinity.

FT-IR spectra, as shown in Fig. 3(a) and (b), were obtained to confirm the presence of surface functional groups on all GQD samples. First, one transmittance peak occurring at *ca.* 1640 cm^{-1} can be assigned to the presence of C═C stretching, which is frequently viewed on N-doped GQDs [33]. Second, one strong peak in the range of 1150–1300 cm^{-1} corresponds to C–O stretch of –COOH, indicating the existence of hydroxyl and carboxyl functional groups [34–36] on GQDs. Third, one transmittance peak appears at approximately 1710 cm^{-1}, mainly originated from the existence of C═N or C═O functional groups [37,38]. Finally, one weak band at *ca.* 3400 cm^{-1} is ascribed to the physically adsorbed water molecules on the surface of GQD samples. From the analysis of FT-IR spectra, all samples possess surface oxygen and nitrogen functional groups, attached to edge or basal plane of GQDs.

XPS measurements were employed to uncover the chemical compositions and distribution of surface functional groups induced by the recipe of chemical precursors. In survey-scan XPS spectra (see Fig. S3), we observe that all GQD samples consist of three elements: C 1s (*ca.* 284 eV), N 1s (*ca.* 400 eV) and O 1s (*ca.* 532 eV) [39,40]. The variation of O/C and N/C atomic ratios with the weight ratio of citric acid to urea is depicted in Fig. 4(a). Both O/C and N/C atomic ratios show a decreasing

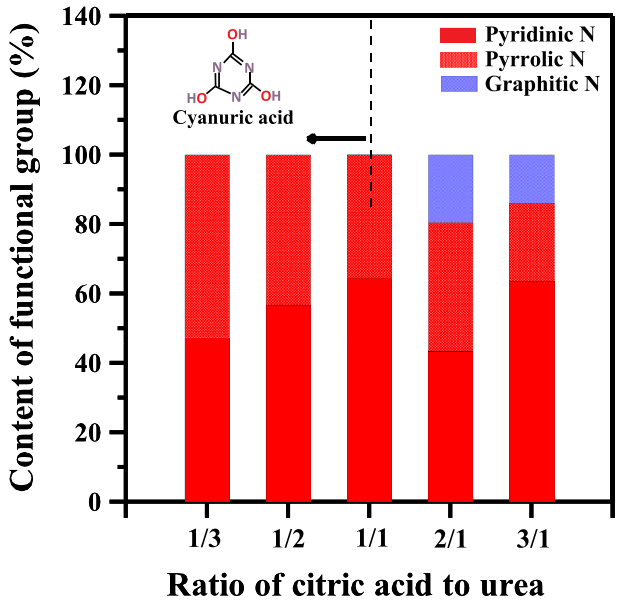

Fig. 5. The distribution of N functionalities on different N-doped GQD samples. Herein the C/U ratio indicates the weight ratio of citric acid to urea.

trend with an increase in the weight ratio. Within the entire range, the O/C ratio shows a slight decreases from 40.3 at.% to 36.5 at.%, whereas the N/C ratio delivers an obvious decreasing trend from 49.6 at.% to 21.6 at.%. The O/C and N/C ratios, as expected, are found to have almost the same magnitude before and after thermal treatment in H_2. This finding reflects that all GQDs contain a resemble oxidation level but different amidation extents.

The distribution of functional groups can be verified by decomposing C 1s and N 1s peaks using a multiple Gaussian function. First, the C 1s spectra were decomposed into five peaks at 284.5 eV (C═C or C–C), 285.8 eV (C═N), 286.6 eV (C–OH), 287.2 eV (O–C═O), and 288.6 eV (C═O), referring to different bonding types to C atoms [40]. As shown in Fig. S4, the portion of C═N group still maintains within a range between 14.1 and 21.3%. This is reasonable because the urea precursor is major contributor to the N content in GQD samples. The N 1s spectra, as illustrated in Fig. 4(e)–4(f), were deconvoluted into three signals, corresponding to predominant pyridinic N (*ca.* 399.2 eV), pyrrolic N (*ca.* 400.2 eV) and quaternary N (*ca.* 401.6 eV) [40]. Generally, the former two component is ascribed to the formation of aromatic C═N–C where N atom tends to bond with two carbon atoms or pyridine moiety, while the last one is assigned to create tertiary N–$(C)_3$ where N atom is bonded to three sp [2] carbon atoms, i.e., graphitic N [41]. The distribution of N functionalities on samples A–E has been collected, as depicted in Fig. 5. The N-functional group distribution of sample A–E is very similar to that of sample F–J. It can be seen that the weight ratio of citric acid to urea at 1:1 is a critical point in affecting the formation of $(CNOH)_3$ and graphitic N. The IRC process at the ratio <1 is prone to crystalline cyanuric acid associated with N-doped GQDs, whereas the IRC process at ratio >1 benefits the creation of graphitic N, accessible for the tendency of in-plane N substitution (i.e., quaternary N) over other in-situ doping steps such as pyrrolic and pyridinic N.

On the basis of experimental results, one schematic diagram for growing N-doped GQDs through the IRC synthesis of citric acid and urea at 200 °C is proposed, as illustrated in Fig. 6. The IRC process is composed of two main steps: (i) thermal pyrolysis of citric acid (melting point: 156 °C) and urea (melting point: 135 °C) and (ii) vapor-phase growth of GQDs and sequent N-doping and O-decorating. In step (i), thermal pyrolysis of carbon precursors is capable of producing a large amount of free radicals such as methyl (CH_3·), hydroxyl (OH·) and amino (NH_2·) radicals under IR irradiation at their decomposition temperatures. The IR induction heat is a radiation that is a simple form of energy without direct energy losses to visible and ultraviolet light [42]. In IR reactor, the near-IR heater arrays are capable of emitting electromagnetic radiation [27]. The radiation power (Q_{ir}) of the IR emitters is proportional to the forth power of the emitter's temperature, based on Stefan-Boltzmann law [43,44].

$$Q_{ir} = A\varepsilon\sigma T^4 \quad (2)$$

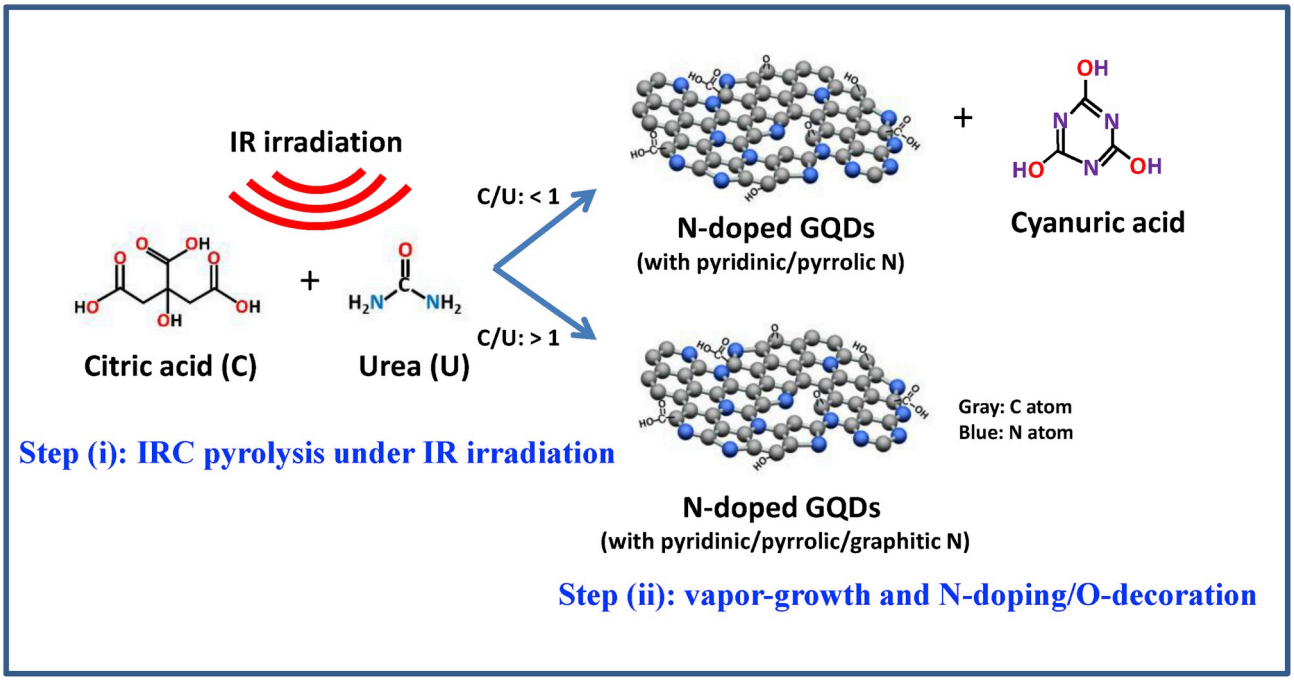

Fig. 6. Schematic diagram illustrating the IRC synthesis of N-doped GQDs, consisted of two steps: (i) thermal pyrolysis under IR irradiation and (ii) vapor-growth and in-situ N-doping/O-decorating. Fig. 5. The distribution of N functionalities on different N-doped GQD samples. Herein the C/U ratio indicates the weight ratio of citric acid to urea.

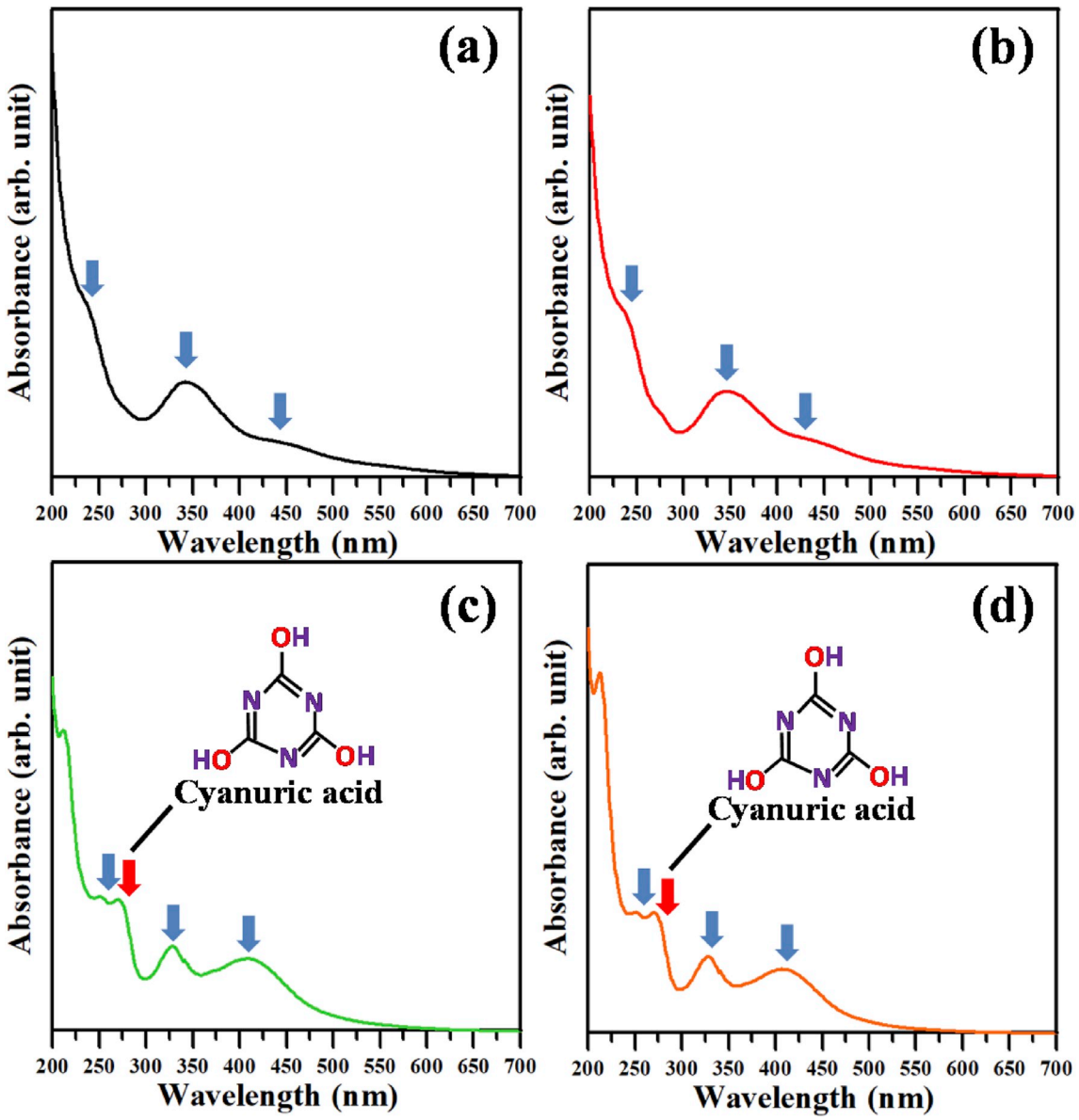

Fig. 7. UV–vis spectra of different N-doped GQDs: (a) A, (b) B, (c) D and (d) E sample.

where A is the surface area of radiating body, ε is the emissivity of radiating body, σ is the Stefan-Boltzmann constant ($= 5.6704 \times 10^{-8}$ W/m [2]·K), and T is the surface absolute temperature. Theoretically, the higher the temperature, the greater is the energy output, and the more efficient is the heat source. The radiant energy could be adsorbed, reflected, and transmitted by the carbon precursors and IR reactor in the reactor. The IRC process is able to offer an efficient heat transfer without contact between the heat source and the carbon precursor, much different to the resistive heating. The spectral distribution of IR energy (E) emitted by a black body can be formulated by Planck's law [44]:

$$E = C_1 \lambda^{-5} / \left(\exp[C_2 / \lambda T] - 1\right) \quad (3)$$

where λ is the wavelength, and C_1 and C_2 are the radiation constants with the values of 3.742×10^8 W μm [4]/m^2 and 1.439×10^4 μm [4] K, respectively. Thus, both the spectral distribution and radiant intensity are strongly governed by the wavelength and emitter temperature. With increasing T or reducing λ, the E value significantly increases within the electromagnetic spectrum of IR range, indicating the importance of type of IR emitters on the efficiency of radiant energy transfer during the ICR process.

In step (ii), the carbon atoms start to build up spherical form of GQDs in vapor phase at this temperature (200 °C). Meanwhile, an in-situ N- and O-decorating or N-doping process also proceed, thus forming sp [2]-hybridized C–N, C–O, C═N and C═O bonds in as-stacked carbon architecture. The GQDs samples are possibly formed through two pathways, related to low and high content of urea precursor. At high urea content, the first pathway leads to the formation of N-doped GQDs and cyanuric acid, while the second one at high citric acid content induces to synthesize N-doped GQDs that consisted of pyridinic/pyrrolic/graphitic N groups. As shown in Fig. 1(d)–1(f), all configurations are prone to form circular peripheries in thermodynamic equilibrium structures to minimize edge free energies, through atomic migration of uncombined and rearrangement of atoms (e.g., C, N, O), and reconstruction of crystallization [45,46].

Three main absorption bands in UV–vis spectra of all GQD suspensions (concentration: 100 mg/L), as shown in Fig. 7, can be viewed within the entire wavelength range from 200 to 450 nm. The absorption bands occur at *ca.* 200–250 nm, 300–350 nm, and 400–450 nm, mainly originated from the presence of π→π* transition of C═C of sp [2]

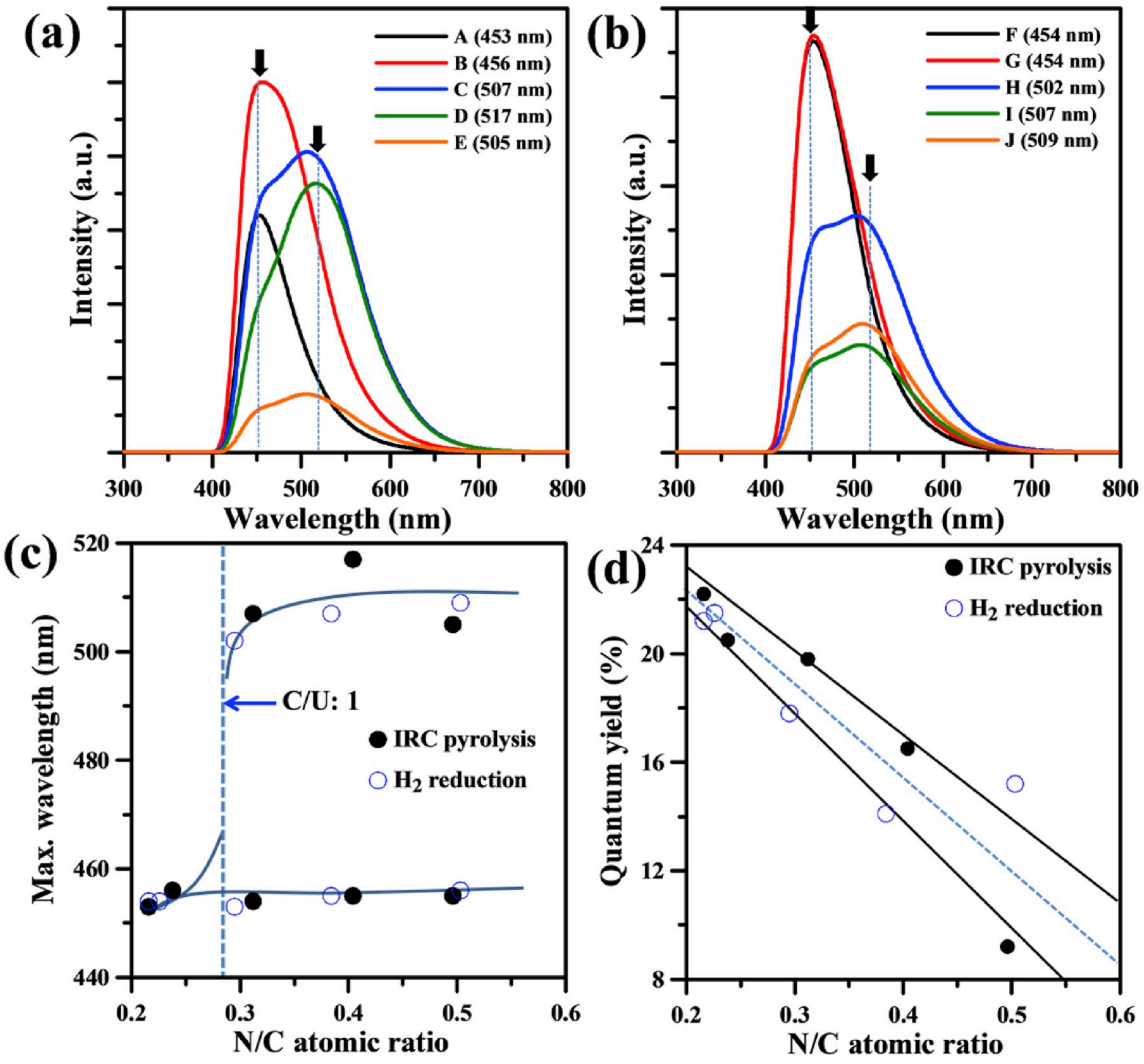

Fig. 8. FL emission spectra of different N-doped GQDs: (a) A–E and (b) F–J sample, excited at 360 nm. Variation of (c) maximal wavelength and (d) quantum yield with the N/C atomic ratio of N-doped GQDs.

domain in sp [3] C matrix, $n\rightarrow\pi^*$ transition of C═O, and surface molecular center or an absorption edge induced by the ($n\rightarrow\pi^*$) transitions of non-bonding electrons of adatoms, respectively [47–49]. It is known that the absorption band can be inferred from the transition state of optical band gap due to the appearance of functional groups (e.g., C═O, C–N, and C═N) [50]. Accordingly, the localization of surface functionalities strongly induces the change of edge of band gap structures. Since all GQD sample behave an identical particle size, it suggests that surface heterogeneity (e.g., localized defect, adatom decoration, chemical bonding) would affect the band-gap configuration of GQDs, thus causing their optical and electrical properties. It is worth noting that C, D, and E samples display an additional band at *ca.* 250 nm, as compared to both A and B samples. This additional absorbance can be attributed to the presence of cyanuric acid, exhibiting a maximum at about 247 nm [51].

Fig. 8(a) and (b) show FL spectra of different GQD suspensions in distilled water excited at 360 nm. It can be seen that both A and B samples displays a quasi-symmetric peak ranging from 400 to 550 nm, whereas C, D, and E samples offers an asymmetric lump, composed of two peaks at *ca.* 450 and 520 nm and a slight tailing from 600 to 700 nm. This FL observation of sample A–E is also identical with that of sample F–J. This reflects that high N/C ratio is favorable for the red-shift behavior.

Fig. S5 shows FL excitation spectrum, where there are three excitation peaks around 320, 335 and 360 nm from sample A. When excited at 360 nm, the N-doped CQDs exhibited strong FL emission centered at *ca.* 475 nm. The photostability of the GQD (i.e., sample A) suspension was performed by after storing all samples more than 3 months. The photoluminescence spectra of all samples under 360 nm before and after 3 months were collected, as shown in Fig. S5. Herein the deviations of photoluminescence intensity for all samples are less than 3.1%, confirming excellent photostability of GQD samples.

As analyzed from Fig. 8(a) and (b), the maximal wavelength varied with the N/C ratio of GDQ samples is illustrated in Fig. 8(c). An obvious red-shift is observed at the N/C atomic ratio of 0.27, i.e., the weight ratio of citric acid to urea: 1:1. This critical point originates from the presence of cyanuric acid that contains a large number of C═N and C–N bonds in the binary crystals, leading to the red-shift behavior. The other concern evaluating the performance of GQDs is η value, which reveals a crucial index to determine the ratio of the number of photon emitted to the number of photon adsorbed during the radiation-induced process [52]. The variation of η value with the N/C atomic ratio is plotted, as shown in Fig. 8(d). The decreasing trend in η value reveals that the photon pathway from high energy adsorbing site to low energy emissive site is possibly retarded due to the presence of cyanuric acid and excessive N and O functional groups at edge sites. This is because the cyanuric acid partially blocks a conjugated π electron transferring through the most probable absorption, thus, resulting in the lower η value. In the words,

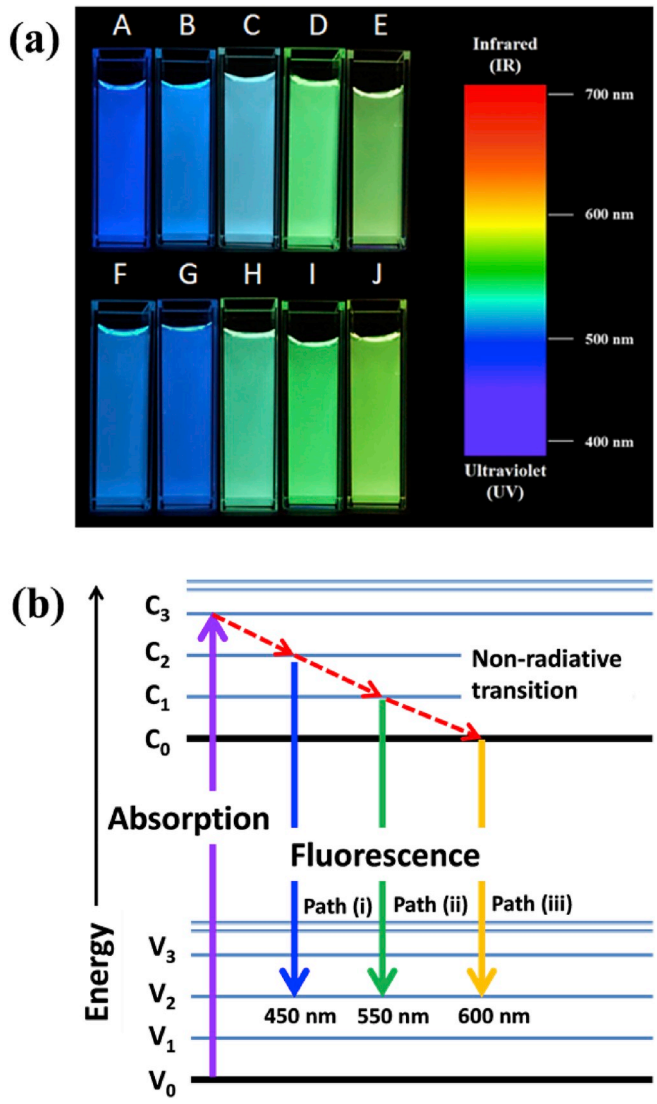

Fig. 9. (a) Photographs of different N-doped GQD suspensions at 360 nm and (b) schematic diagram of different electronic transitions on N-doped GQD suspensions.

both D and E sample contain a number of deactivated zigzag-edge sites and ineffective energy transfer between N-/O-dopants and carbon surface [53]. In contrast, both A and B samples are found to exhibit high η values of 22.2 and 20.5%, respectively. The substitutional N (i.e., graphitic or quaternary N) in both A and B samples can serve as an essential role in more effective radiative emission. The highly efficient FL emission mainly originates from high electron-withdrawing possibility [33] without excessive N- and O-rich edge groups as major contributors in inducing the FL quenching. A comparison of η values form different GQD samples prepared by the IRC method and previous techniques was given. The η values of N-doped GQDs are 15.7% (from hydrothermal synthesis folic acid and ethylene glycol at 180 °C) [54], 32.4% (from hydrothermal synthesis of citric acid and dicyandiamide at 180 °C) [55], 3.0% (from thermal pyrolysis of ethylene glycol at 185 °C) [56], and 23.3% (from thermal pyrolysis of citric acid at 200 °C) [57]. For comparison, the synthesized GQDs prepared from the pyrolysis of citric acid + urea under IR irradiation exhibit quite comparable and/or better optical properties than other reported GQDs from various carbon precursors and heat sources.

The optical photographs of all GQD suspensions in distilled water under UV illumination (365 nm) are collected, as shown in Fig. 9(a). Under the UV light, the GQD suspensions can emit different lights: deep blue (sample A), blue, (sample B), blue-green (sample C), green (sample D), and bright green (sample E). This color transition of all samples is well identical with the analysis of FL spectra. Since C, D and E samples possess a number of crystalline cyanuric acid, this specie can be slightly dissolved in water, thus enhancing the FL intensity at a wavelength of approximately 526 nm [58]. This is presumably one possible reason that the FL spectra of D and E samples emit a multiple emission within a wider wavelength range, as compared to that of sample A and B.

As depicted in Fig. 8(a) and (b), a multiple FL intensity level of GQDs was observed. Accordingly, a schematic diagram of different electronic transitions on GQD suspensions is proposed, as shown in Fig. 9(b), where the individual transitions are indicated by arrows in a multiple chromophoric band-gap structure [14,59]. The doping of O and N atoms enables the creation of defect sites that introduce other energy levels and new electron transition pathways in inter-band structure of GQDs [38]. Under UV irradiation, the absorption of UV photons by the localized π electron in double bonds (mainly C═C) produces an electron–hole pair (exciton) after electron transition. The exciton may emit blue light (path (i)) through radiative recombination after vibration relaxation. The excited electron possibly undergoes inter-band transition from a higher conduction band to a lower conduction band, subsequently emitting green and yellow light (path (ii) and (iii)) by radiative recombination [40]. Herein path (i), (ii) and (iii) can be considered as radiative recombination from different excited states: C_{π^*}, O_{π^*} and N_{π^*}, respectively. Due to their highly atomic heterogeneity on all GQDs, the excited electrons are believed to undergo simultaneously the three pathways. This inter-band structure provides an explanation why the GQD samples emit an asymmetric FL emission spectrum under 360-nm UV irradiation. As to the presence of cyanuric acid, this specie possibly offers an additional UV-absorption path, resulting in other extra FL emissions, e.g., an additional emission at *ca.* 520 nm (see an arrow in Fig. 8(a) and (b)). Accordingly, this unique inter-band structure, induced by the co-existence of N-doped GQD and cyanuric acid, significantly causes a complicated and wide FL emission and an obvious tailing effect in the wavelength range. Thus, the appearance of cyanuric acid is unfavorable for emitting monochrome light with a narrow full-width at half maximum. According to the deduction, A and B samples can be considered as a monochrome light under an appropriate light illumination (i.e., mainly path (i)), whereas the rest samples can be taken into account as an emitter for a whole wavelength light source (i.e., path (i), (ii) and (iii)), e.g., white light-emitting-diode device.

4. Conclusions

An efficient IRC technique has been developed to grow N-doped GQDs through thermal pyrolysis of citric acid and urea. High production yield of 43.2 wt% GQDs was achieved by the IRC synthesis method using the precursor with the ratio of citric acid to urea: 3:1. The GQDs were found to form an equilibrium shapes of circle with an average particle size ranged from 5 to 10 nm. The weight ratio of chemical precursor could serve as a crucial factor in controlling the crystallinity, functional group distribution and chemical composition of as-prepared GQDs. With increasing the urea content, the GQDs not only contain N-doped graphene but also incorporate with crystalline cyanuric acid, forming a binary crystallinity. The N/C atomic ratio in the GQDs could precisely tailored in a range from 21.6 to 49.6 at.% by simply controlling the weight ratio of citric acid to urea. The quantum yield of N-doped GQDs could attain as high as 22.2%. Excessive N and cyanuric acid imparted FL quenching, red shift and wide spectral distribution. One multiple chromophoric band-gap structure, having three pathways from different radiative sites, was proposed to describe the FL spectra of GQD samples. The graphitic N (A and B samples) served as an essential role in more effective radiative emission, whereas the presence of cyanuric acid (D and E samples) was unfavorable for emitting monochrome light with a narrow full-width at half maximum. Accordingly, we have demonstrated

an effective and inspiring IRC approach to engineering both chemical compositions and unique crystalline structures of GQDs, benefiting basic research and applications to optical, sensing, energy and biological fields in the near future.

Acknowledgments

Financial support from the Ministry of Science and Technology of Taiwan (Contact No.: MOST 108-2221-E-155-036-MY3) is greatly acknowledged.

Appendix A. Supplementary data

Supplementary data to this article can be found online at https://doi.org/10.1016/j.jlumin.2019.116774.

References

[1] K.S. Novoselov, A.K. Geim, S.V. Morozov, D. Jiang, Y. Zhang, S.V. Dubonos, I. V. Grigorieva, A.A. Firsov, Electric field effect in atomically thin carbon films, Science 306 (2004) 666–669.
[2] S. Stankovich, D.A. Dikin, G.H.B. Dommett, K.M. Kohlhaas, E.J. Zimney, E. A. Stach, R.D. Piner, S.T. Nguyen, R.S. Ruoff, Graphene-based composite materials, Nature 442 (2006) 282.
[3] X. Li, X. Wang, L. Zhang, S. Lee, H. Dai, Chemically derived, ultrasmooth graphene nanoribbon semiconductors, Science 319 (2008) 1229–1232.
[4] J. Shen, Y. Zhu, X. Yang, C. Li, Graphene quantum dots: emergent nanolights for bioimaging, sensors, catalysis and photovoltaic devices, Chem. Commun. 48 (2012) 3686–3699.
[5] S.H. Sun, L. Wu, W. Wei, X. Qu, Recent advances in graphene quantum dots for sensing, Mater. Today 16 (11) (2013) 433–442.
[6] L. Li, G. Wu, G. Yang, J. Peng, J. Zhao, J.-J. Zhu, Focusing on luminescent graphene quantum dots: current status and future perspectives, Nanoscale 5 (2013) 4015–4039.
[7] Z. Zhang, J. Zhang, N. Chen, L. Qu, Graphene quantum dots: an emerging material for energy-related applications and beyond, Energy Environ. Sci. 5 (2012) 8869–8890.
[8] S. Bak, D. Kim, H. Lee, Graphene quantum dots and their possible energy applications: a review, Curr. Appl. Phys. 16 (2016) 1192–1201.
[9] D. Pan, C. Xi, Z. Li, L. Wang, Z. Chen, B. Lu, M. Wu, Electrophoretic fabrication of highly robust, efficient, and benign heterojunction photoelectrocatalysts based on graphene-quantum-dot sensitized TiO_2 nanotube arrays, J. Mater. Chem. A 1 (2013) 3551–3555.
[10] Z. Zhu, J. Ma, Z. Wang, C. Mu, Z. Fan, L. Du, Y. Bai, L. Fan, H. Yan, D.L. Phillips, S. Yang, Efficiency enhancement of perovskite solar cells through fast electron extraction: the role of graphene quantum dots, J. Am. Chem. Soc. 136 (2014) 3760–3763.
[11] D. Chao, C. Zhu, X. Xia, J. Liu, X. Zhang, J. Wang, P. Liang, J. Lin, H. Zhang, Z. X. Shen, H.J. Fan, Graphene quantum dots coated VO_2 arrays for highly durable electrodes for Li and Na ion batteries, Nano Lett. 15 (2015) 565–573.
[12] L. Ruiyi, J. Yuanyuan, Z. Xiaoyan, L. Zaijun, G. Zhiguo, W. Guangli, L. Junkang, Significantly enhanced electrochemical performance of lithium titanate anode for lithium ion battery by the hybrid of nitrogen and sulfur Co-doped graphene quantum dots, Electrochim. Acta 178 (2015) 303–311.
[13] H. Yu, Y. Zhao, C. Zhou, L. Shang, Y. Peng, Y. Cao, L.-Z. Wu, C.-H. Tung, T. Zhang, Carbon quantum dots/TiO_2 composites for efficient photocatalytic hydrogen evolution, J. Mater. Chem. A 2 (2014) 3344–3351.
[14] D. Qu, M. Zheng, P. Du, Y. Zhou, L. Zhang, D. Li, H. Tan, Z. Zhao, Z. Xie, Z. Sun, Highly luminescent S, N Co-doped graphene quantum dots with broad visible absorption bands for visible light photocatalysts, Nanoscale 5 (2013) 12272–12277.
[15] H.M.R. Gonçalves, A.J. Duarte, J.C.G. Esteves da Silva, Optical fiber sensor for Hg (II) based on carbon dots, Biosens. Bioelectron. 26 (2010) 1302–1306.
[16] S.-T. Yang, L. Cao, P.G. Luo, F. Lu, X. Wang, H. Wang, M.J. Meziani, Y. Liu, G. Qi, Y.-P. Sun, Carbon dots for optical imaging in vivo, J. Am. Chem. Soc. 131 (2009) 11308–11309.
[17] R. Atchudan, T.N.J.I. Edison, S. Perumal, N. Clament Sagaya Selvam, Y.R. Lee, Green synthesized multiple fluorescent nitrogen-doped carbon quantum dots as an efficient label-free optical nanoprobe for in vivo live-cell imaging, J. Photochem. Photobiol., A 372 (2019) 99–107.
[18] R. Atchudan, T.N.J.I. Edison, K.R. Aseer, S. Perumal, N. Karthik, Y.R. Lee, Highly fluorescent nitrogen-doped carbon dots derived from Phyllanthus acidus utilized as A fluorescent probe for label-free selective detection of Fe^{3+} oons, live cell imaging and fluorescent ink, Biosens. Bioelectron. 99 (2018) 303–311.
[19] R. Atchudan, T.N.J.I. Edison, K.R. Aseer, S. Perumal, Y.R. Lee, Hydrothermal conversion of magnolia liliiflora into nitrogen-doped carbon dots as an effective turn-off fluorescence sensing, multi-colour cell imaging and fluorescent ink, Colloids Surf., B 169 (2018) 321–328.
[20] T. Pal, S. Mohiyuddin, G. Packirisamy, Facile and green synthesis of multicolor fluorescence carbon dots from curcumin: in vitro and in vivo bioimaging and other applications, ACS Omega 3 (2018) 831–843.
[21] R. Atchudan, T.N.J.I. Edison, S. Perumal, R. Vinodh, Y.R. Lee, In-situ green synthesis of nitrogen-doped carbon dots for bioimaging and TiO_2 Nanoparticles@ Nitrogen-doped carbon composite for photocatalytic degradation of organic pollutants, J. Alloy. Comp. 766 (2018) 12–24.
[22] T.N.J.I. Edison, R. Atchudan, M.G. Sethuraman, J.-J. Shim, Y.R. Lee, Microwave assisted green synthesis of fluorescent N-doped carbon dots: cytotoxicity and bio-imaging applications, J. Photochem. Photobiol., B 161 (2016) 154–161.
[23] J. Ju, R. Zhang, W. Chen, Photochemical deposition of surface-clean silver nanoparticles on nitrogen-doped graphene quantum dots for sensitive colorimetric detection of glutathione, Sens. Actuators, B 228 (2016) 66–73.
[24] S.K. Bhunia, A. Saha, A.R. Maity, S.C. Ray, N.R. Jana, Carbon nanoparticle-based fluorescent bioimaging probes, Sci. Rep. 3 (2013) 1473.
[25] Y. Xu, M. Wu, Y. Liu, X.-Z. Feng, X.-B. Yin, X.-W. He, Y.-K. Zhang, Nitrogen-doped carbon dots: a facile and general preparation method, photoluminescence investigation, and imaging applications, Chem. Eur. J. 19 (2013) 2276–2283.
[26] X. Gao, C. Du, Z. Zhuang, W. Chen, Carbon quantum dot-based nanoprobes for metal ion detection, J. Mater. Chem. C 4 (2016) 6927–6945.
[27] C.-T. Hsieh, Y.-F. Chen, C.-T. Pai, C.-Y. Mo, Synthesis of lithium nickel cobalt manganese oxide cathode materials by infrared induction heating, J. Power Sources 269 (2014) 31–36.
[28] J. Peng, W. Gao, B.K. Gupta, Z. Liu, R. Romero-Aburto, L. Ge, L. Song, L. B. Alemany, X. Zhan, G. Gao, S.A. Vithayathil, B.A. Kaipparettu, A.A. Marti, T. Hayashi, J. Zhu, P.M. Ajayan, Graphene quantum dots derived from carbon fibers, Nano Lett. 12 (2012) 844–849.
[29] C.-T. Hsieh, C.-Y. Lin, Y.-F. Chen, J.-S. Lin, H. Teng, Silver nanorods attached to graphene sheets as anode materials for lithium-ion batteries, Carbon 62 (2013) 109–116.
[30] Y.T. Lee, N.S. Kim, J. Park, J.B. Han, Y.S. Choi, H. Ryu, H.J. Lee, Temperature-dependent growth of carbon nanotubes by pyrolysis of ferrocene and acetylene in the range between 700 and 1000°C, Chem. Phys. Lett. 372 (2003) 853–859.
[31] K. Kim, K. Kim, W.S. Jung, S.Y. Bae, J. Park, J. Choi, J. Choo, Investigation on the temperature-dependent growth rate of carbon nanotubes using chemical vapor deposition of ferrocene and acetylene, Chem. Phys. Lett. 401 (2005) 459–464.
[32] L. Ni, K. Kuroda, L. Zhou, T. Kizuka, K. Ohta, K. Matsuishi, J. Nakamura, Kinetic study of carbon nanotube synthesis over Mo/Co/MgO catalysts, Carbon 44 (2006) 2265–2272.
[33] L. Tang, R. Ji, X. Cao, J. Lin, H. Jiang, X. Li, K.S. Teng, C.M. Luk, S. Zeng, J. Hao, S. P. Lau, Deep ultraviolet photoluminescence of water-soluble self-passivated graphene quantum dots, ACS Nano 6 (2012) 5102–5110.
[34] P. Russo, A. Hu, G. Compagnini, W.W. Duley, N.Y. Zhou, Femtosecond laser ablation of highly oriented pyrolytic graphite: a green route for large-scale production of porous graphene and graphene quantum dots, Nanoscale 6 (2014) 2381–2389.
[35] B.P. Vinayan, Z. Zhao-Karger, T. Diemant, V.S.K. Chakravadhanula, N. I. Schwarzburger, M.A. Cambaz, R.J. Behm, C. Kübel, M. Fichtner, Performance study of magnesium–sulfur battery using a graphene based sulfur composite cathode electrode and a non-nucleophilic Mg electrolyte, Nanoscale 8 (2016) 3296–3306.
[36] Z. Yang, Z. Yao, G. Li, G. Fang, H. Nie, Z. Liu, X. Zhou, X.a. Chen, S. Huang, Sulfur-doped graphene as an efficient metal-free cathode catalyst for oxygen reduction, ACS Nano 6 (2012) 205–211.
[37] A. Periasamy, S. Muruganand, M. Palaniswamy, Vibrational studies of Na_2SO_4, K_2SO_4, $NaHSO_4$ and $KHSO_4$ crystals, Rasayan J. Chem. 2 (2009) 981–989.
[38] P. Kharangarh, S. Umapathy, G. Singh, Thermal effect of sulfur doping for luminescent graphene quantum dots, ECS J. Solid State Sci. Technol. 7 (2018) M29–M34.
[39] Z. Jin, J. Yao, C. Kittrell, J.M. Tour, Large-scale growth and characterizations of nitrogen-doped monolayer graphene sheets, ACS Nano 5 (2011) 4112–4117.
[40] L. Tang, R. Ji, X. Li, G. Bai, C.P. Liu, J. Hao, J. Lin, H. Jiang, K.S. Teng, Z. Yang, S. P. Lau, Deep ultraviolet to near-infrared emission and photoresponse in layered N-doped graphene quantum dots, ACS Nano 8 (2014) 6312–6320.
[41] C.K. Chen, Z. Chai, C. Li, L. Shi, M. Liu, Q. Xie, Y. Zhang, D. Xu, A. Manivannan, Z. Liu, Catalyst-free growth of three-dimensional graphene flakes and graphene/g-C_3N_4 composite for hydrocarbon oxidation, ACS Nano 10 (2016) 3665–3673.
[42] C.-T. Hsieh, C. Pan, W.-Y. Chen, Synthesis of silver nanoparticles on carbon papers for electrochemical catalysts, J. Power Sources 196 (2011) 6055–6061.
[43] P. Gao, G. Yang, H. Liu, L. Wang, H. Zhou, Lithium diffusion behavior and improved high rate capacity of $LiNi_{1/3}Co_{1/3}Mn_{1/3}O_2$ as cathode material for lithium batteries, Solid State Ion. 207 (2012) 50–56.
[44] R. Siegel, J.R. Howell, Thermal Radiation Heat Transfer, Taylor & Francis Group, Press, New York, 2002.
[45] T. Xu, K. Yin, X. Xie, L. He, B. Wang, L. Sun, Size-dependent evolution of graphene nanopores under thermal excitation, Small 8 (2012) 3422–3426.
[46] X. Jia, M. Hofmann, V. Meunier, B.G. Sumpter, J. Campos-Delgado, J.M. Romo-Herrera, H. Son, Y.-P. Hsieh, A. Reina, J. Kong, M. Terrones, M.S. Dresselhaus, Controlled formation of sharp zigzag and armchair edges in graphitic nanoribbons, Science 323 (2009) 1701–1705.
[47] M. Xu, G. He, Z. Li, F. He, F. Gao, Y. Su, L. Zhang, Z. Yang, Y. Zhang, A green heterogeneous synthesis of N-doped carbon dots and their photoluminescence applications in solid and aqueous states, Nanoscale 6 (2014) 10307–10315.
[48] T.-F. Yeh, W.-L. Huang, C.-J. Chung, I.T. Chiang, L.-C. Chen, H.-Y. Chang, W.-C. Su, C. Cheng, S.-J. Chen, H. Teng, Elucidating quantum confinement in graphene oxide dots based on excitation-wavelength-independent photoluminescence, J. Phys. Chem. Lett. 7 (2016) 2087–2092.

[49] F. Liu, M.-H. Jang, H.D. Ha, J.-H. Kim, Y.-H. Cho, T.S. Seo, Facile synthetic method for pristine graphene quantum dots and graphene oxide quantum dots: origin of blue and green luminescence, Adv. Mater. 25 (2013) 3657–3662.
[50] D. Qu, M. Zheng, J. Li, Z. Xie, Z. Sun, Tailoring color emissions from N-doped graphene quantum dots for bioimaging applications, Light. Sci. Appl. 4 (2015) e364.
[51] I.M. Klotz, T. Askounis, Absorption spectra and tautomerism of cyanuric acid, melamine and some related compounds, J. Am. Chem. Soc. 69 (1947) 801–803.
[52] J.R. Lakowicz, Principles of Fluorescence Spectroscopy, Kluwer Academic Plenum, 1999.
[53] F. Schedin, A.K. Geim, S.V. Morozov, E.W. Hill, P. Blake, M.I. Katsnelson, K. S. Novoselov, Detection of individual gas molecules adsorbed on graphene, Nat. Mater. 6 (2007) 652.
[54] R. Zhang, W. Chen, Nitrogen-doped carbon quantum dots: facile synthesis and application as a "turn-off" fluorescent probe for detection of Hg^{2+} ions, Biosens. Bioelectron. 55 (2014) 83–90.
[55] J. Ju, R. Zhang, S. He, W. Chen, Nitrogen-doped graphene quantum dots-based fluorescent probe for the sensitive turn-on detection of glutathione and its cellular imaging, RSC Adv. 4 (2014) 52583–52589.
[56] X. Gao, Y. Lu, R. Zhang, S. He, J. Ju, M. Liu, L. Li, W. Chen, One-pot synthesis of carbon nanodots for fluorescence turn-on detection of Ag^{+} based on the Ag^{+}-induced enhancement of fluorescence, J. Mater. Chem. C 3 (2015) 2302–2309.
[57] J. Ju, W. Chen, Synthesis of highly fluorescent nitrogen-doped graphene quantum dots for sensitive, label-free detection of Fe (III) in aqueous media, Biosens. Bioelectron. 58 (2014) 219–225.
[58] G. Liu, Y. She, S. Hong, J. Wang, D. Xu, Development of ELISA-like fluorescence assay for melamine detection based on magnetic dummy molecularly imprinted polymers, Appl. Sci. 8 (2018) 560–572.
[59] X. Li, S.P. Lau, L. Tang, R. Ji, P. Yang, Sulphur doping: a facile approach to tune the electronic structure and optical properties of graphene quantum dots, Nanoscale 6 (2014) 5323–5328.